Simulated WSR-88D Velocity and Reflectivity Signatures of Numerically Modeled Tornadoes

VINCENT T. WOOD AND RODGER A. BROWN

NOAA/National Severe Storms Laboratory, Norman, Oklahoma

DAVID C. DOWELL*

NOAA/National Severe Storms Laboratory, and Cooperative Institute for Mesoscale Meteorological Studies, University of Oklahoma, Norman, Oklahoma

(Manuscript received 3 June 2008, in final form 2 December 2008)

ABSTRACT

Low-altitude radar reflectivity measurements of tornadoes sometimes reveal a donut-shaped signature (low-reflectivity eye surrounded by a high-reflectivity annulus) and at other times reveal a high-reflectivity knob associated with the tornado. The differences appear to be due to such factors as (i) the radar's sampling resolution, (ii) the presence or absence of lofted debris and a low-reflectivity eye, (iii) whether measurements were made within the lowest few hundred meters where centrifuged hydrometeors and smaller debris particles were recycled back into the tornadic circulation, and (iv) the presence or absence of multiple vortices in the parent tornado.

To explore the influences of some of these various factors on radar reflectivity and Doppler velocity signatures, a high-resolution tornado numerical model was used that incorporated the centrifuging of hydrometeors. A model reflectivity field was computed from the resulting concentration of hydrometeors. Then, the model reflectivity and velocity fields were scanned by a simulated Weather Surveillance Radar-1988 Doppler (WSR-88D) using both the legacy resolution and the new super-resolution sampling. Super-resolution reflectivity and Doppler velocity data are displayed at 0.5° instead of 1.0° azimuthal sampling intervals and reflectivity data are displayed at 0.25-km instead of 1.0-km range intervals.

Since a mean Doppler velocity value is the reflectivity-weighted mean of the radial motion of all the radar scatterers within a radar beam, a nonuniform distribution of scatterers produces a different mean Doppler velocity value than does a uniform distribution of scatterers. Nonuniform reflectivities within the effective resolution volume of the radar beam can bias the indicated size and strength of the tornado's core region within the radius of the peak tangential velocities. As shown in the simulation results, the Doppler-indicated radius of the peak wind underestimates the true radius and true peak tangential velocity when the effective beamwidth is less than the tornado's core diameter and there is a weak-reflectivity eye at the center of the tornado. As the beam becomes significantly wider than the tornado's core diameter with increasing range, the peaks of the Doppler velocity profiles continue to decrease in magnitude but overestimate the tornado's true radius. With increasing range from the radar, the prominence of the weak-reflectivity eye at the center of the tornado is progressively lessened until it finally disappears. As to be expected, the Doppler velocity signatures and reflectivity eye signatures were more prominent and stronger with super-resolution sampling than those with legacy-resolution sampling.

1. Introduction

Radar reflectivity measurements made in tornadoes near the radar reveal the presence of weak-echo holes that coincide with the center of the tornado vortex. The hole or eye is surrounded by a ring or annulus of high reflectivities forming a donut-shaped signature. The eye arises from the centrifuging of debris and hydrometeors within the tornadic circulation, as simulated in the high-

* Current affiliation: National Center for Atmospheric Research, Boulder, Colorado.

Corresponding author address: Vincent Wood, NOAA/National Severe Storms Laboratory, 120 David L. Boren Blvd., Norman, OK 73072.
E-mail: vincent.wood@noaa.gov

DOI: 10.1175/2008JTECHA1181.1

resolution tornado numerical model of Dowell et al. (2005, hereafter D05). Fujita (1981) and Fujita and Wakimoto (1982) document weak-echo holes coincident with the locations of tornadoes within 10 km of a Weather Surveillance Radar-1957 (WSR-57). Using the National Severe Storms Laboratory's (NSSL) 10.6-cm-wavelength, high-resolution (0.5° azimuthal sampling interval and 150-m range spacing) Doppler radar, Lemon et al. (1982) and Johnson and Ziegler (1984) found that weak-echo holes at about 70-km range were coincident with tornadic vortex signatures (e.g., Brown et al. 1978) and extended from low altitudes to the top of the storm. The hole differed from a bounded weak-echo region in that it was smaller and it was not capped by high reflectivities at upper altitudes, but extended uninterrupted to just beneath the storm summit.

Wakimoto and Martner (1992) use high-resolution proximity single-Doppler radar measurements and photographs to compare the detailed structural relationship of a tornado's reflectivity (including a low-reflectivity eye) and Doppler velocity fields with its visual features. Wakimoto et al. (1996, 2003) show that the presence of a weak-echo eye in airborne Doppler radar observations is coincident with photographic documentation of the tornado center. Proximity radar observations of tornadoes by mobile, high-resolution Doppler radars reveal details about the three-dimensional structure of the tornado vortex, including (a) spiral bands of high reflectivities surrounding a low-reflectivity eye and (b) a tapering of a high-reflectivity annulus toward the surface, both of which are coincident with the center of the vortex (Wurman et al. 1996; Bluestein and Pazmany 2000; Wurman and Gill 2000; Wurman 2002; Wurman and Alexander 2004; Wurman and Samaras 2004; Alexander and Wurman 2005; Bluestein et al. 2003; Bluestein 2005; D05; Bluestein et al. 2007).

D05 speculate that raindrops, and sometimes debris, are the usual scatterers observed by radar in a tornado's high-reflectivity annulus. With their high-resolution tornado numerical model, they demonstrate that the centrifuging of hydrometeors and debris produces a minimum in the number of particles within the vortex core and produces a maximum in a surrounding annulus.

WSR-88D observations of the 3 May 1999 Oklahoma City, Oklahoma, tornado (which produced F5 damage), however, revealed a prominent ''knob'' in the hook echo at the lowest elevation angles when the tornado passed relatively close (15–60 km) to the Twin Lakes, Oklahoma (KTLX), and the Radar Operations Center, Norman, Oklahoma (KCRI), WSR-88D sites (Burgess et al. 2002). The knob signature represents a local region of high reflectivities including debris coincident with the center of the tornado vortex at low altitudes. While the tornado was passing through populated areas, the high-reflectivity maximum in the knob extended upward to a few kilometers in height. After the tornado exited the areas, reflectivity within the knob decreased. On the same day, two high-resolution, 3-cm-wavelength, mobile Doppler on Wheels (DOW) radars observed the same tornado at very close range (2–8 km) and revealed on some occasions the presence of a weak-reflectivity eye and on other occasions a strong-reflectivity knob coincident with the center of the tornado vortex (Burgess et al. 2002).

Since a mean Doppler velocity value is the reflectivity-weighted mean of the radial motion of all the radar scatterers within the radar beam, it is not clear how the nonuniform distribution of scatterers within a tornado affects the distribution of Doppler velocity values across the tornado relative to the true distribution of the tangential velocity values. We attempt to resolve this issue by using a WSR-88D emulator to simulate Doppler velocity and reflectivity measurements within three tornadic circulations that had been generated by the high-resolution tornado numerical model of D05. Both the WSR-88D legacy- and super-resolution sampling modes are employed to produce simulated Doppler velocity and reflectivity measurements. The resolution of the data that has been collected since the installation of WSR-88Ds during the 1990s is referred to as ''legacy'' resolution. Super-resolution reflectivity and Doppler velocity data are displayed at 0.5° instead of 1.0° azimuthal sampling intervals and the reflectivity data are displayed at 0.25-km instead of 1.0-km range intervals.

2. Approach

a. Description of tornado numerical model

D05 employ a high-resolution tornado numerical model to study particle motions and concentrations in tornadoes. The model, similar to the Fiedler (1993) numerical model, consists of two-dimensional, axisymmetric forced convection inside a closed, impermeable cylinder that rotates at a constant angular velocity. Ideally, this represents a rotating updraft within which the initial vertical vorticity is concentrated to produce a tornadic circulation. The governing equations in the numerical model were solved on a uniform Cartesian grid having radial and vertical spacings that differed among the simulated tornadoes. The top, bottom, and radial sides of the domain were rigid with no-slip boundary conditions.

D05 demonstrate how an initially uniform distribution of precipitation particles and debris objects responds to vortex airflow. They employ a number of simplifying assumptions, including that the precipitation

TABLE 1. Parameters used to initialize the simulations for experiments I, II, and III.

Parameter	EXP I	EXP II	EXP III
Radial extent of the domain (R, km)	3	10	10
Vertical extent of the domain (H, km)	5	10	10
Grid spacings (Δr and Δh, m)	10 and 10	25 and 25	25 and 25
Angular velocity (Ω, $\times 10^{-3}$ s^{-1})	2.5	10	10
Maximum buoyancy (B_o, m s^{-2})	1.31	1.31	0.653
Bottom height of the forcing region (h_b, m)	0	0	1000
Top height of the forcing region (h_t, m)	4000	8000	9000
Radius of the forcing region (r_B, m)	500	500	1500
CAPE (J kg^{-1})	3300	6600	3300
Diffusion coefficient (ν, m^2 s^{-1})	25	50	50

particles do not coalesce or break up and do not affect the airflow. The drag coefficient for debris is assumed to be isotropic and independent of object-relative airspeed that characterizes an object's drag properties when falling at its terminal velocity.

Since raindrop sizes within real tornadoes are unknown, D05 use a range of raindrop sizes to determine the degree of accumulation of hydrometeors in a surrounding annulus and the rate of expansion of the annulus in the vortex region. They find that (a) smaller raindrops (0.5-mm diameter) are centrifuged but contribute less to total reflectivity than larger drops and (b) larger raindrops (≥5 mm diameter) are centrifuged too far away from the vortex center.

For this study, we chose a drop diameter of 1.5 mm (corresponding to a terminal fall velocity of 5.4 m s^{-1}) to produce a reasonably sized high-reflectivity annulus. Terminal fall velocity, based on the laboratory experiments of Gunn and Kinzer (1949), was assumed to be constant with height, because the air density in the idealized numerical model is constant throughout the domain. With time, the centrifuging of raindrops by the vortex airflow produced a minimum concentration of drops at the center of the vortex and a maximum concentration in an annulus surrounding the center. Model reflectivity values, Z_m (mm^6 m^{-3}), were computed from the raindrop concentrations by using the relationship (Battan 1973)

$$Z_m = nD^6, \quad (1)$$

where n is the number of drops per cubic meter and D is the uniform drop diameter (1.5 mm). For the 1.5-mm-diameter raindrops, the specified initial concentration of raindrops (8.779 m^{-3}) produced a uniform model reflectivity field of 100 mm^6 m^{-3} or 20 dBZ. The evolving numerical vortex then redistributed the raindrops to produce tornado-like reflectivity fields.

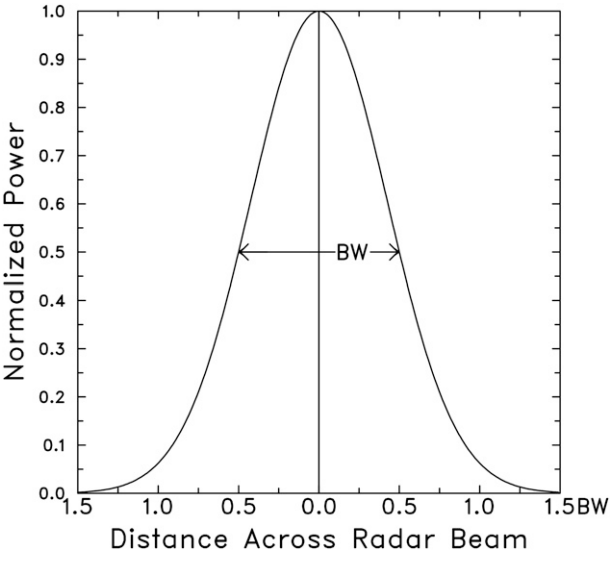

FIG. 1. Normalized power across the symmetric main lobe of a WSR-88D is approximated by the Gaussian distribution. The half-power beamwidth is indicated by BW. The portion of the main lobe of the beam used in our computations was 3 times the half-power beamwidth. [After Brown et al. (2002a).]

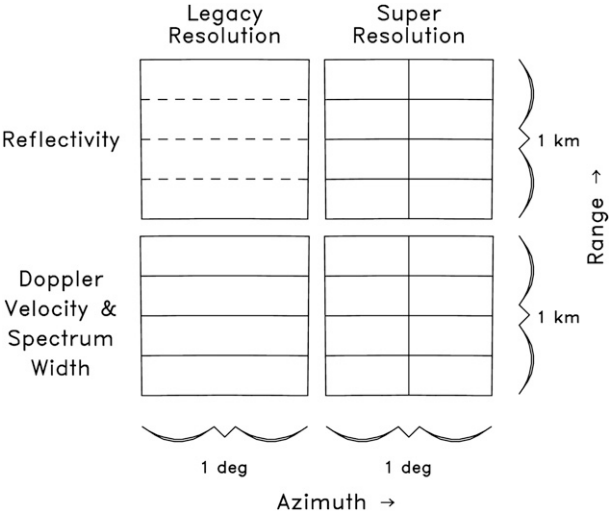

FIG. 2. Size of range bins (azimuthal width across page, pulse length up page) for (left) legacy WSR-88D resolution and (right) super-resolution at a range of 60 km from the radar. Dashed lines in the legacy reflectivity rectangle (1° × 1 km) indicate that four adjacent range bins of nonmissing reflectivity values are averaged to produce the recorded and displayed reflectivity value. [After Brown et al. (2005).]

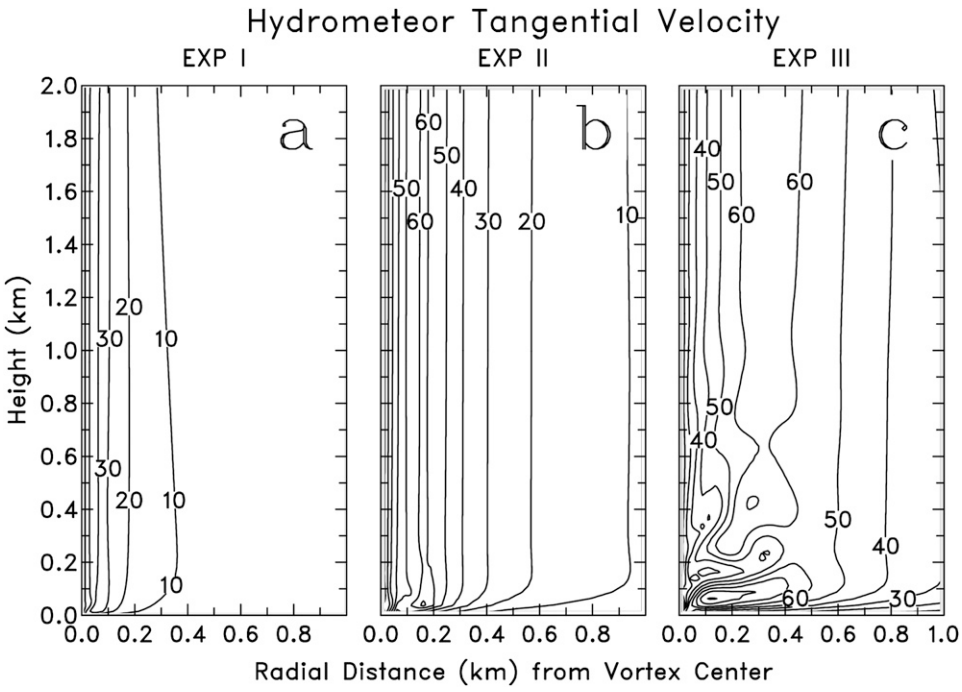

FIG. 3. Hydrometeor (1.5-mm raindrop) tangential velocity (m s^{-1}) fields from experiments (a) I (medium tornado), (b) II (large tornado), and (c) III (very large tornado) normal to the vertical plane through the center of the vortex. The EXP I, II, and III results, respectively, are shown after 600, 1100, and 500 s of model integration when the vortices were most intense.

We used the numerical model to produce flow and reflectivity patterns for three different-sized tornadoes. Different updraft and vortex intensities were produced in the three experiments by varying the maximum buoyancy (B_o), the radius of the forcing region (r_B), the bottom (h_b) and top heights (h_t) of the forcing region, the angular velocity (Ω), the radial and vertical grid spacings (Δr and Δh), and the diffusion coefficient (ν) (see Table 1 for the list of parameter values used for the three experiments). The buoyancy distribution specified by D05 is given by

$$B(r,h) = B_o \cos\left(\frac{\pi r}{2r_B}\right) \sin\left[\pi\left(\frac{h-h_b}{h_t-h_b}\right)\right], \quad 0 \le r \le r_B, \quad \text{and} \quad h_b \le h \le h_t, \quad \text{or} \quad (2a)$$

$$B(r,h) = 0, \text{otherwise.} \quad (2b)$$

Convective available potential energy (CAPE) along the central axis is given by

$$\text{CAPE} = 2B_o\left(\frac{h_t-h_b}{\pi}\right). \quad (3)$$

We used the same values for other parameters that were used in the D05 simulations.

b. WSR-88D radar emulator

WSR-88D Doppler velocity and reflectivity measurements of the model tornadoes were simulated using a Doppler radar emulator that reproduced the basic characteristics of a WSR-88D. Several simplifications, however, were employed. Instead of the radar beam consisting of a main lobe and sidelobes, it consisted only of a main lobe that was represented by a Gaussian distribution. The width of the beam typically is specified by the half-power beamwidth, which is the angular width of the beam where the power was one-half of the peak power at the center of the beam (Fig. 1).

Instead of averaging radar pulses to produce simulated mean Doppler velocity and reflectivity values, the mean Doppler velocity and mean reflectivity factor

TABLE 2. Peak rotational velocities and core diameters for the medium (EXP I), large (EXP II), and very large (EXP III) tornadoes.

	Peak velocity (m s^{-1})		Core diameter (m)	
EXP	Lowest 100 m	Aloft	Lowest 100 m	Aloft
I	40	32	110	150
II	72	62	330	330
III	92	64	230	680

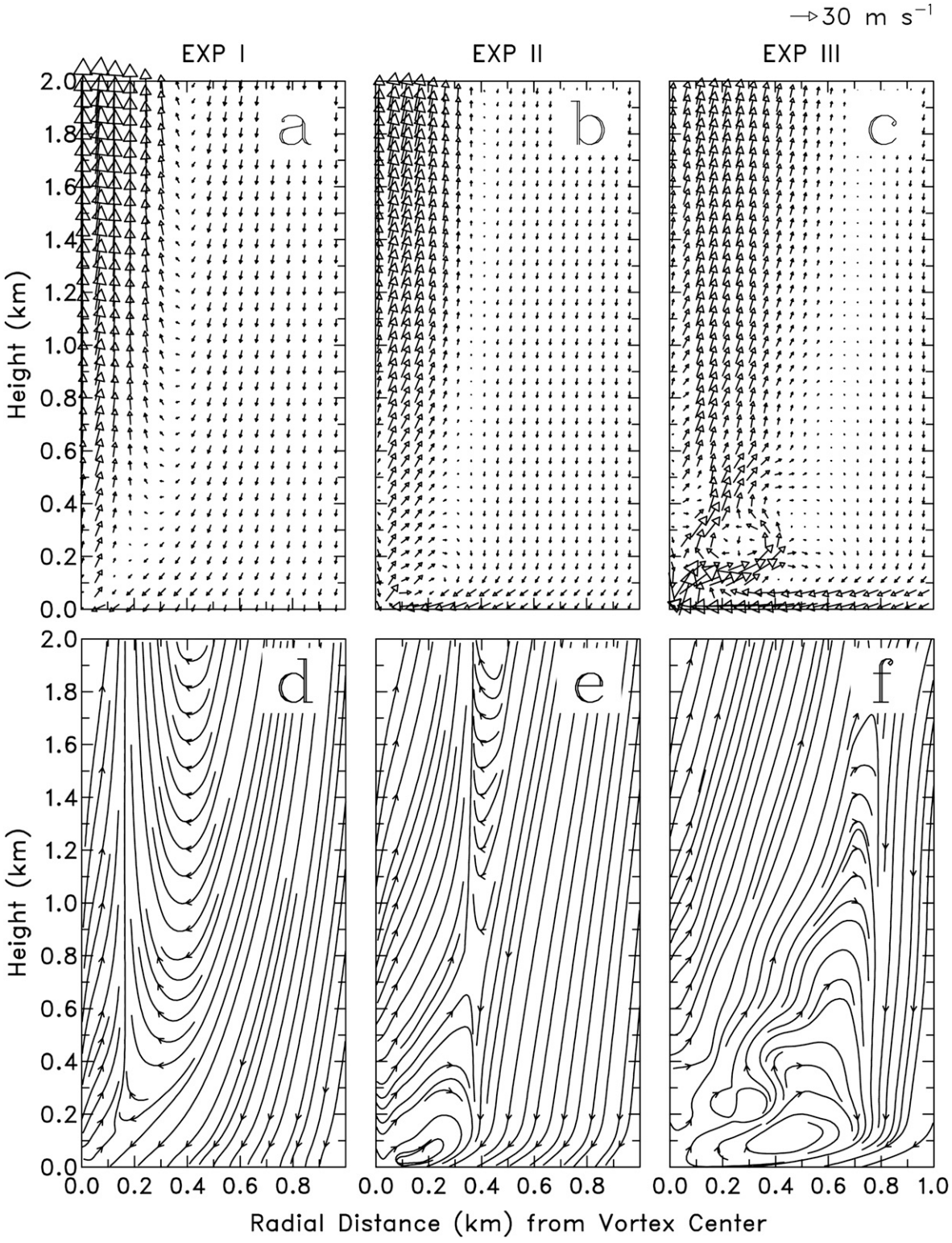

FIG. 4. Hydrometeor (1.5-mm raindrop) (a)–(c) velocity vectors and (d)–(f) streamlines from experiments I, II, and III within a vertical plane passing through the center of the vortex. A velocity vector of 30 m s^{-1} is indicated.

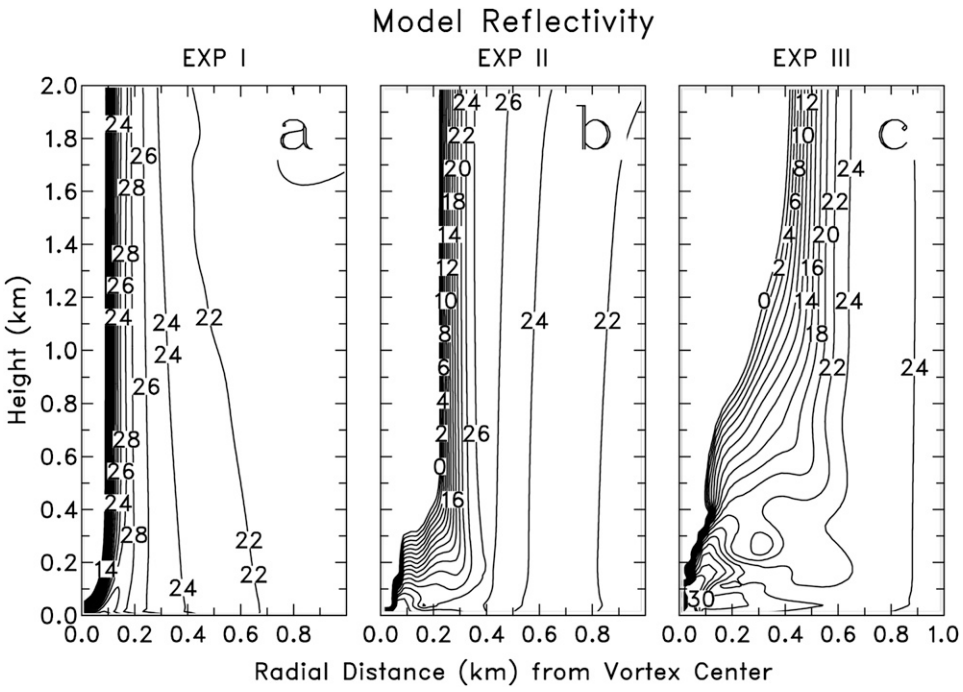

FIG. 5. Same as in Fig. 3, but for model reflectivity (dB*Z*) fields. Values less than 0 dB*Z* in the eye are not contoured.

were computed by averaging distributed model hydrometeor motion and reflectivity values, respectively, within the beam. Hydrometeor motion and reflectivity values were obtained by linearly interpolating three-dimensional, gridded model velocity components and reflectivity factors based on raindrop concentrations produced by the D05 model. When the lower portion of the beam was below the ground, the mean Doppler velocity and reflectivity values were computed only for that portion of the beam above the ground. A brief description of the calculation of the volume-averaged Doppler velocity and reflectivity values within the main lobe is found in the appendix. Test computations indicated that this faster approach was a very good approximation to the averaging of successive pulses.

For a scanning radar, the antenna can move a significant fraction of the angular beamwidth during the time it takes to collect the required number of samples to estimate the radar parameters within a specific azimuthal sampling interval. As a consequence, the circular beam of the WSR-88D is essentially broadened in the direction of antenna rotation, producing a larger ''effective'' horizontal beamwidth. For the WSR-88D simulations in this study, we used the average WSR-88D antenna half-power beamwidth of 0.89°. As indicated in Fig. 1 of Brown et al. (2002b), when super-resolution data are collected at 0.5° azimuthal sampling intervals (ΔAZ), the antenna beamwidth is broadened to an effective beamwidth of 1.02°. For ΔAZ of 1.0° traditionally used by WSR-88Ds (referred to in this paper as *legacy resolution*), the effective beamwidth is a much broader 1.39°. The procedure for computing the simulated effective beamwidth is discussed in Brown et al. (2002b).

Doppler radar data were simulated using the two different spatial resolutions: (a) legacy resolution and (b) super-resolution. The transmitted pulse length for both the reflectivity and Doppler velocity is 0.25 km (illustrated schematically on the left side of Fig. 2). However, before legacy reflectivity values are displayed and recorded, nonmissing reflectivity values from four consecutive pulse lengths (indicated by horizontal dashed lines in Fig. 2) are averaged to produce data that represent a coarser 1.0-km range interval.

According to Wood et al. (2001) and Brown et al. (2002b), WSR-88D detections of mesocyclones and tornadoes can be improved by collecting super-resolution data at a smaller azimuthal sampling interval of 0.5° and at the original 0.25-km pulse length (right side of Fig. 2). Additionally, Brown et al. (2005) find that actual reflectivity and Doppler velocity signatures in severe storms are more clearly depicted with super-resolution data. The capability to process super-resolution data at lower-elevation angles is now available on WSR-88Ds.

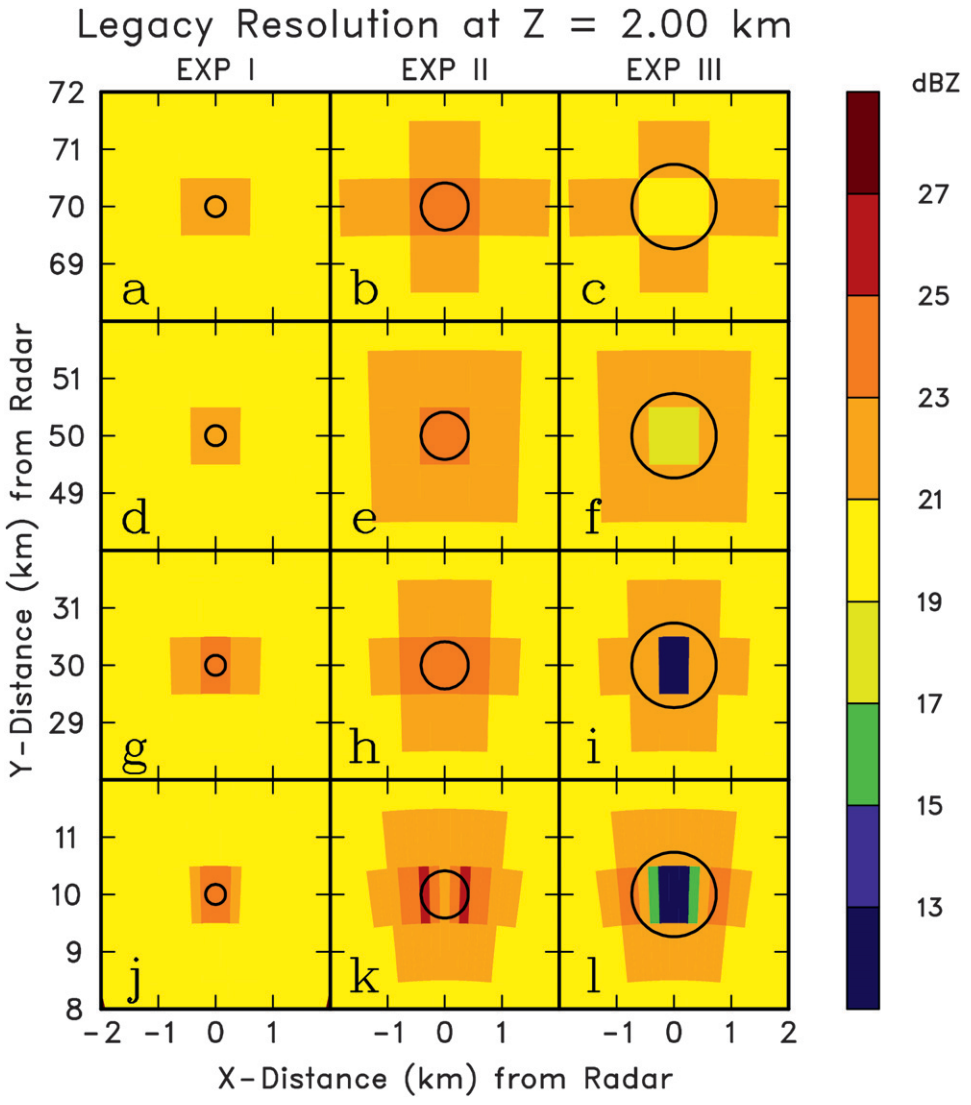

FIG. 6. Horizontal views of simulated WSR-88D reflectivity signatures measured by a radar located 10, 30, 50, and 70 km from a model weak-reflectivity eye at 2.0-km height for the three tornadoes (EXPs I–III). Patterns in all panels represent legacy-resolution data displayed at 1.0° azimuthal intervals and 1.0-km range intervals. The solid circle represents the true annulus of high reflectivity outside the vortex core. The radar is located beyond the bottom of the figure.

3. Tornado model numerical simulation results

The D05 numerical model was used to produce the radial, tangential, and vertical components of raindrop motion and reflectivity [computed from the concentration of raindrops using Eq. (1)]. Three different-sized tornadoes were created using the model. In experiment I (EXP I), a medium-sized tornado was produced. Several attempts were made to form a smaller tornado that had a core diameter (diameter of the peak tangential velocities) in the 50–100-m category by varying the model's input parameters while using grid characteristics similar to those in the other experiments. Although these attempts were unsuccessful, it should be feasible to simulate small tornadoes in future studies by employing higher resolution and/or a somewhat more sophisticated tornado model. Instead, we settled for a tornado that had a core diameter aloft (i.e., above 100 m AGL, where the vortex characteristics are more uniform in the vertical) of 150 m and a peak hydrometeor tangential velocity of 32 m s^{-1} (Fig. 3). In experiment II (EXP II), the large vortex having a peak velocity of 62 m s^{-1} and a core diameter of 330 m was produced. In experiment III (EXP III), a rare very large tornado

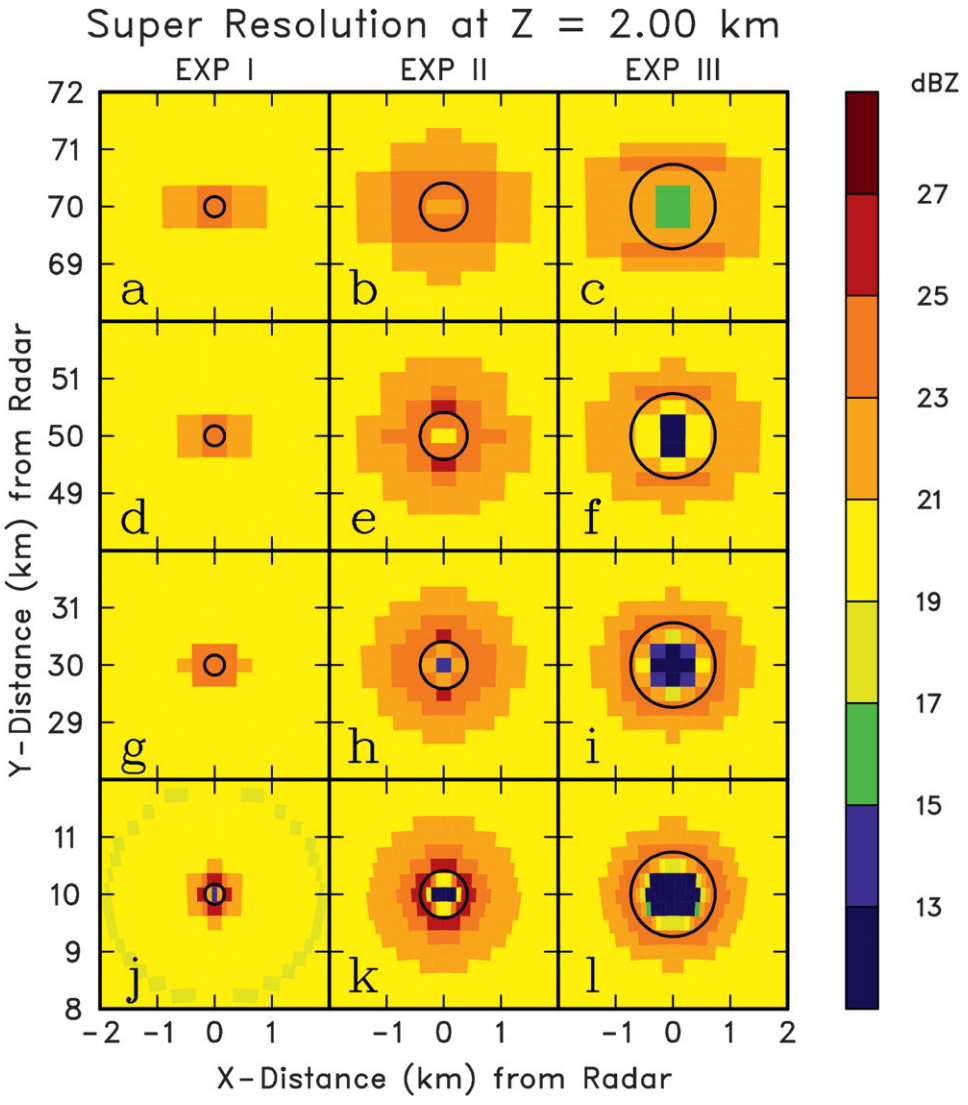

FIG. 7. Same as in Fig. 6, but for super-resolution data displayed at 0.5° azimuthal intervals and 0.25-km range intervals.

having a core diameter aloft of 680 m and peak hydrometeor tangential velocity of 64 m s^{-1} was generated. These peak rotational velocities and core diameters are consistent with the DOW-based climatology of supercell tornado structures and dynamics (Alexander and Wurman 2008).

Table 2 summarizes these peak rotational velocities and core diameters aloft above the lowest 100 m as well as those in the lowest 100 m for the three tornadoes. It is worth noting that the lower portion of the very large tornado in EXP III had a peak tangential velocity of 92 m s^{-1} with a core diameter of 230 m at a height of 60 m.

The hydrometeor velocity vectors and streamlines within the three vortices are shown in Fig. 4. While being lifted by the updraft, the 1.5-mm-diameter hydrometeors were centrifuged outward relative to the air and moved at a speed that was less than the air in the tangential direction (not shown). Thus, centrifuging of raindrops produced a low-reflectivity eye inside the vortex core region and a high-reflectivity annulus outside the core region (Fig. 5). Some descending raindrops outside the core were drawn into the updraft by strong surface inflow winds, thereby resulting in the recycling of the drops. Recycling of raindrops was more pronounced with the very large vortex (EXP III; Figs. 4c and 4f) than with the large vortex (EXP II; Figs. 4b and 4e), as indicated by higher reflectivities in the lower few hundred meters (Figs. 5b and 5c). The recycling process is not present in EXP I, owing to the weaker inflow at low altitudes (Figs. 4a and 4d).

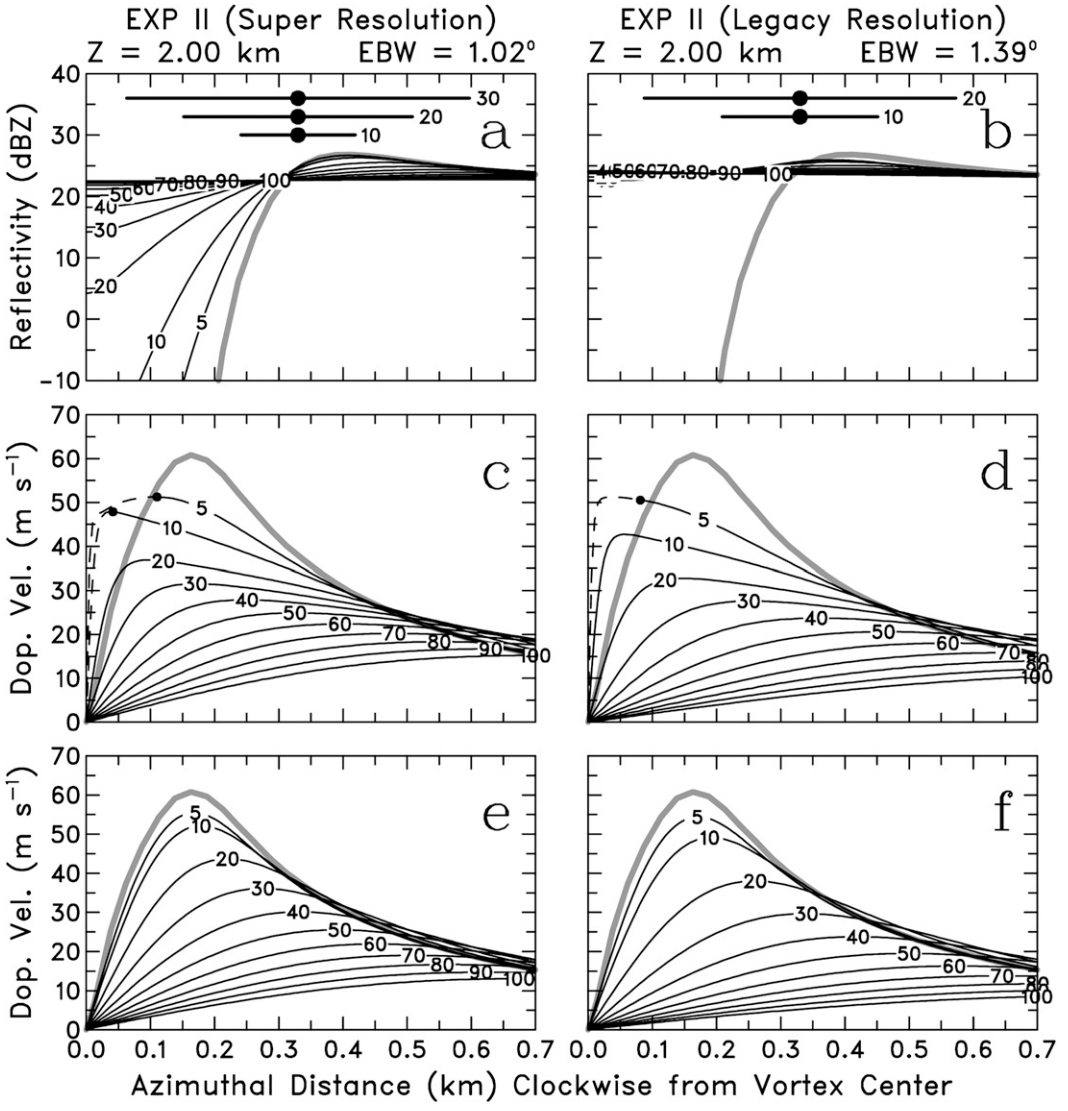

FIG. 8. Radial profiles of mean Doppler velocity and reflectivity from the tornado center for the large tornado (EXP II) at a height of 2.0 km and a variety of ranges from the simulated radar. The thick gray curves represent radial profiles of (a),(b) reflectivity computed directly from the model raindrop concentration and (c)–(f) the tangential velocity of the model raindrops. The horizontal lines with a centered black dot in the upper portions of (a) and (b) represent the effective half-power beamwidths associated with (left) $\Delta AZ = 0.5°$ and (right) $\Delta AZ = 1.0°$ at the specified ranges (km). The black curves in (a) and (b) represent azimuthal profiles of radar reflectivity measurements at a number of different ranges (km) based on model reflectivity values as if the radar sampled the tornado in a continuous manner in an azimuthal direction. In (c) and (d), the black curves represent Doppler velocity measurements computed from the model tangential velocity values and simulated nonuniform reflectivity values. (e),(f) Doppler velocity measurements calculated directly from the model tangential velocity values and a uniform reflectivity value of 20 dBZ that represents the initial concentration of raindrops in the D05 model. The small black dot between the solid and dashed portions of the curves in the middle panels represents the MDR value below which Doppler velocity values cannot be computed (see MDR discussion in the appendix). The dashed portions of those curves represent the theoretical azimuthal profiles of Doppler velocity that would have been measured if there were no minimum detectable reflectivity value.

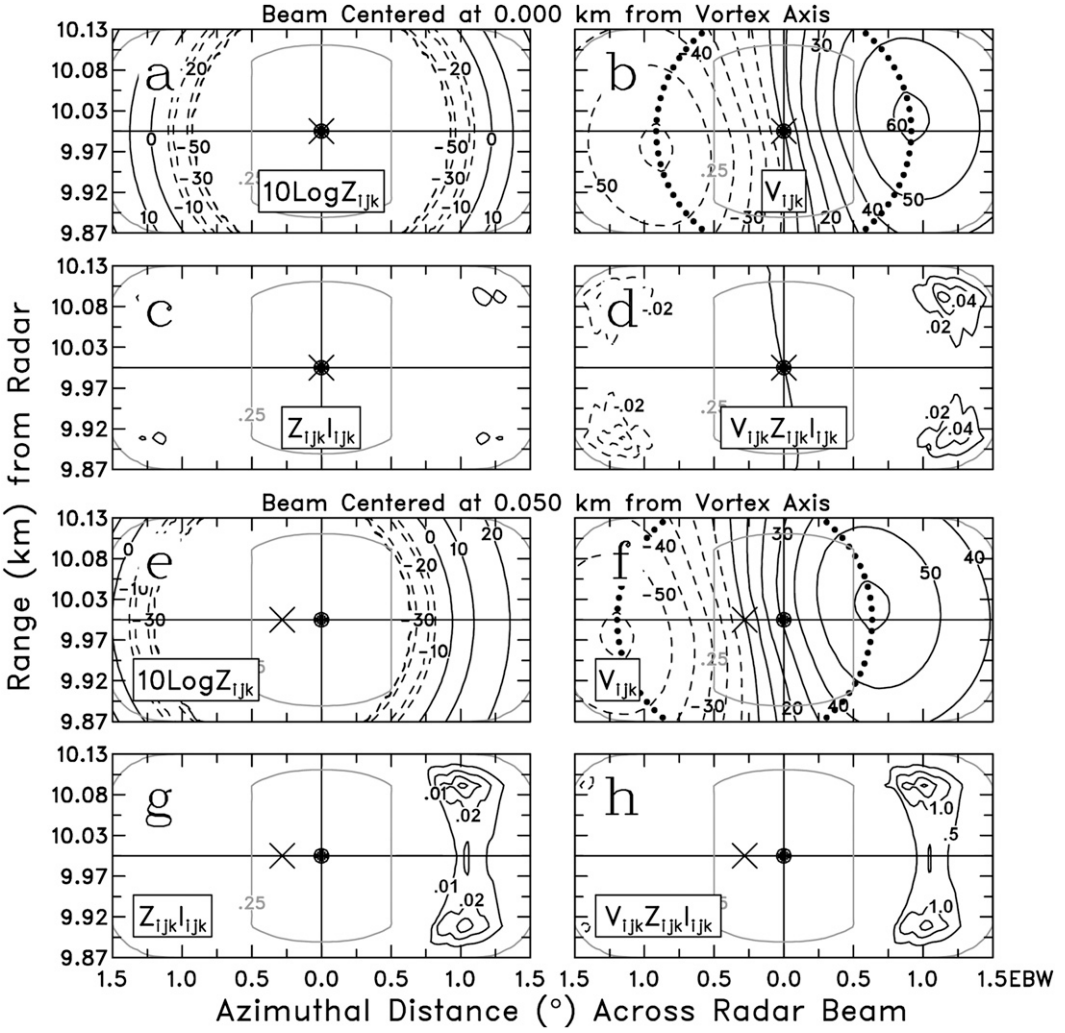

FIG. 9. Horizontal cross section of the effective radar beam at 10-km range with the center of the beam (black dot) (a)–(d) coincident with the center of the EXP II vortex (×) and (e)–(h) located 0.05 km in a clockwise direction from the vortex center. Fields shown in (a) and (e) are the reflectivity (10 log Z_{ijk}, dBZ), (b) and (f) the undegraded Doppler velocity (V_{ijk}, m s^{-1}), (c) and (g) the product of the reflectivity factor (Z_{ijk}) and the composite antenna-weighting function (I_{ijk}) of the antenna beam pattern (mm^6 m^{-3}), and (d) and (h) the product of V_{ijk}, Z_{ijk}, and I_{ijk} (mm^6 m^{-2} s^{-1}). Dashed (solid) curves indicate negative (positive) contours. The composite antenna-weighting function is normalized to 1.0 at the center of the beam; gray contours represent normalized two-way antenna-weighting values of 0.25 and approximately 0.0. The dotted black circle centered on the × represents the location of the true maximum hydrometeor tangential velocity in (b) and (f). The Doppler velocity peaks in (b) and (f) are not at the same range from the radar because hydrometeor motion in the vortex was slightly divergent.

4. Influence of nonuniform scatterer distributions on radar measurements

a. Influence of a weak-reflectivity eye on reflectivity measurements

The model velocity and reflectivity outputs from the D05 numerical model were scanned with the WSR-88D emulator to produce simulated legacy- and super-resolution Doppler radar measurements in the three tornadoes. In Figs. 6 and 7, displays of simulated legacy-resolution WSR-88D reflectivity donut-shaped signatures at 2-km height are compared as a function of range with displays showing super-resolution signatures. It is assumed that the radar beam is centered on the weak-reflectivity eyes of three different-sized tornadoes. Owing to the widening radar beam with increasing range, the radar reflectivity signatures are progressively degraded with increasing range. With legacy-resolution data collection (Fig. 6), a weak knob is associated with the EXP I tornado at ranges of 20 km and greater because the radar

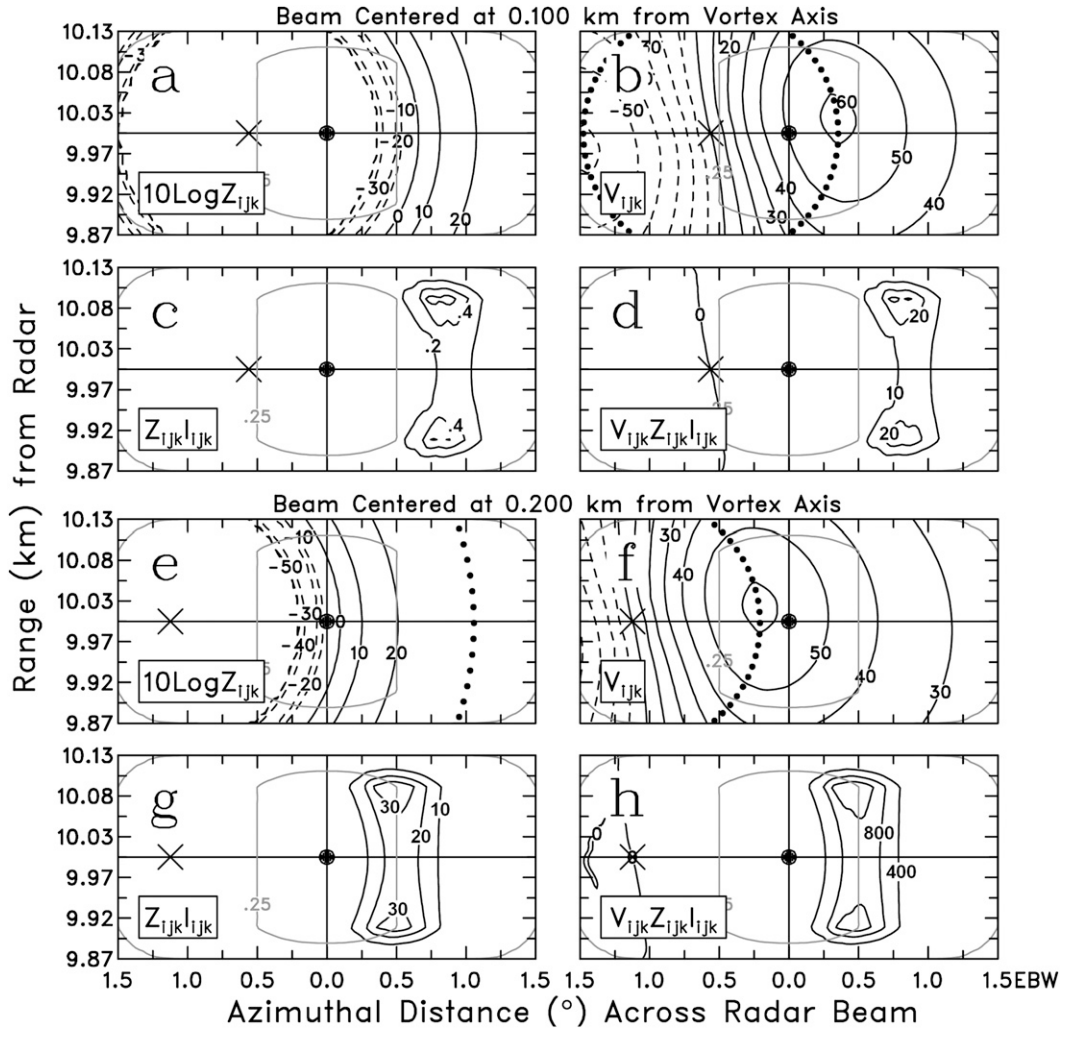

FIG. 10. Same as in Fig. 9, but for the beam axis located (a)–(d) 0.1 and (e)–(h) 0.2 km clockwise from the tornado center. The dotted black circle in (e) represents the location of the true maximum reflectivity in the annulus.

beam is much larger than the tornado's weak-reflectivity eye. For the large EXP II tornado, there is a donut signature at 10-km range and a weak knob at greater ranges. With the very large tornado of EXP III, the basic characteristics of the model reflectivity field (Fig. 5) are evident. The tornado's wide eye produces a donut reflectivity signature that slowly degrades with increasing range. The donut signature (Fig. 6i) resembles the simulated WSR-88D signature of the weak-reflectivity eye at 32 km from the DOW radar that has been reconstructed from DOW observations of the 12 May 2004 Harper, Kansas, tornado at low altitudes (Wurman and Alexander 2004).

With super-resolution data collection (Fig. 7), all of the reflectivity signatures are more pronounced and more circular at a given range than with legacy WSR-88D data collection (Fig. 6). For the EXP I tornado, a weak donut is evident up through 30-km range. For the EXP II tornado, the donut is obvious to a range of less than 70 km. The donut signature associated with the EXP III tornado is much stronger and more circular than with legacy radar resolution.

If the radar beam, for instance, is located at some distance offset from the weak-reflectivity eye, the donut signature becomes less pronounced. Wood and Brown (1997, 2000) showed that the random position of the beam can change the magnitudes and locations of peak Doppler velocity values. The important implication is that short-term variations in tornado intensity and reflectivity structures may be due to (a) the chance positioning of the radar beam relative to the vortex's maximum rotational velocities or the weak-reflectivity eye, (b) evolution, or (c) some combination of both.

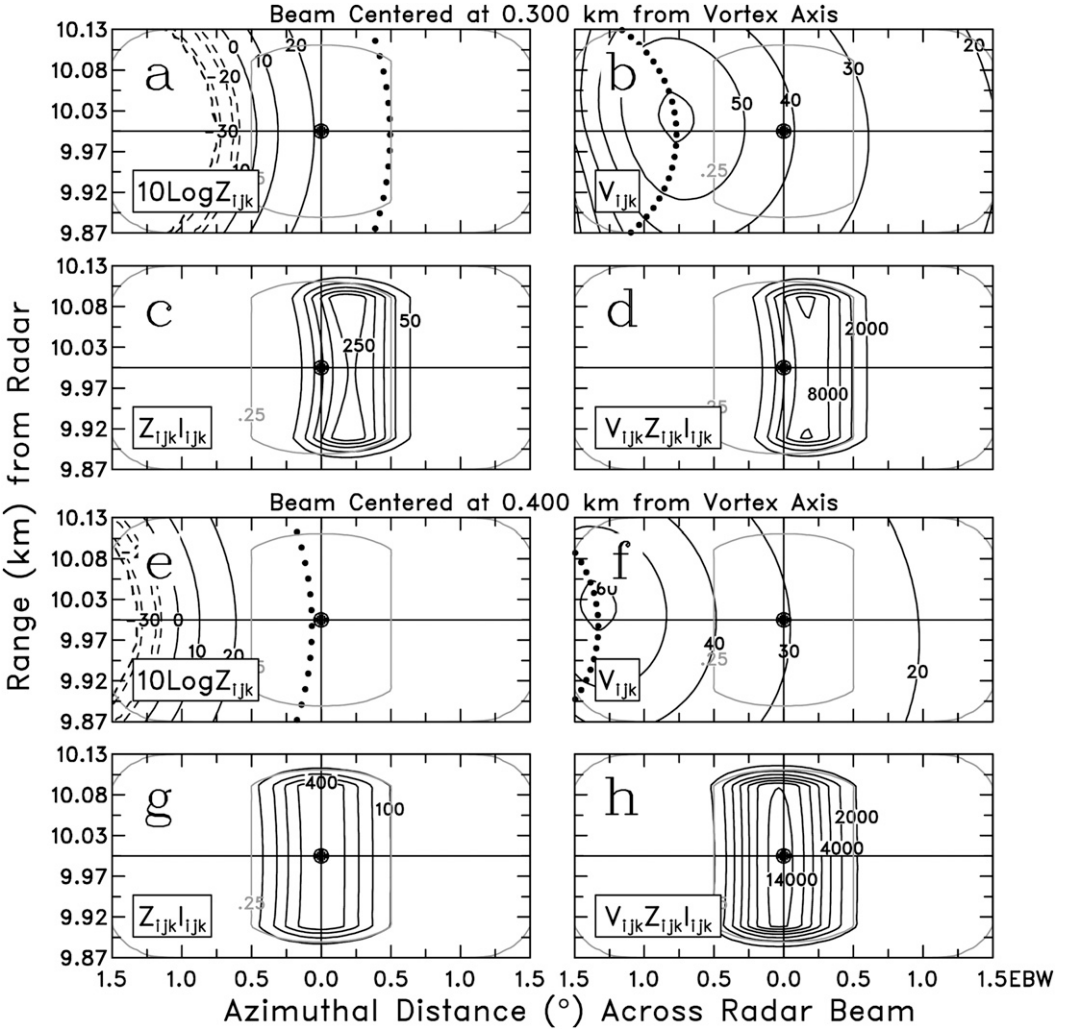

FIG. 11. Same as in Fig. 9, but for the beam axis located (a)–(d) 0.3 and (e)–(h) 0.4 km clockwise from the tornado center. The dotted black circles in (a) and (e) represent the locations of the true maximum reflectivities in the annulus.

b. *Influence of a weak-reflectivity eye on Doppler velocity measurements*

As an introduction to the influence of the distribution of radar scatterers on Doppler velocity measurements across a tornado, Fig. 8 was prepared. Examples of simulated Doppler velocity and reflectivity profiles in the radial direction from the center of the EXP II tornado for the two Doppler radar data resolutions are presented at a height of 2.0 km and at various ranges from the simulated radar. To present continuous Doppler velocity and reflectivity profiles, values were calculated as if the radar were able to make measurements at infinitesimally small azimuth intervals.

If the radar beamwidth and pulse length were zero (i.e., perfect resolution), Doppler velocity and reflectivity measurements would have perfectly reproduced the model tangential velocity and reflectivity values in the tornado, as indicated by the thick, gray curves in Fig. 8. However, with nonzero pulse lengths and effective beamwidths of 1.02° for super-resolution azimuthal sampling (left side of Fig. 8) and 1.39° for legacy sampling (right side), reflectivity and Doppler velocity profiles become degraded, and increasingly so, as the beam broadens with increasing range from the radar.

With super-resolution sampling of the EXP II vortex, the weak-reflectivity eye and higher-reflectivity annulus (Fig. 8a) gradually disappear with increasing range, transforming essentially into a uniform reflectivity field beyond about 50-km range. In contrast, the reflectivity field produced by legacy-resolution sampling is nearly uniform at all ranges (Fig. 8b). The reason for the

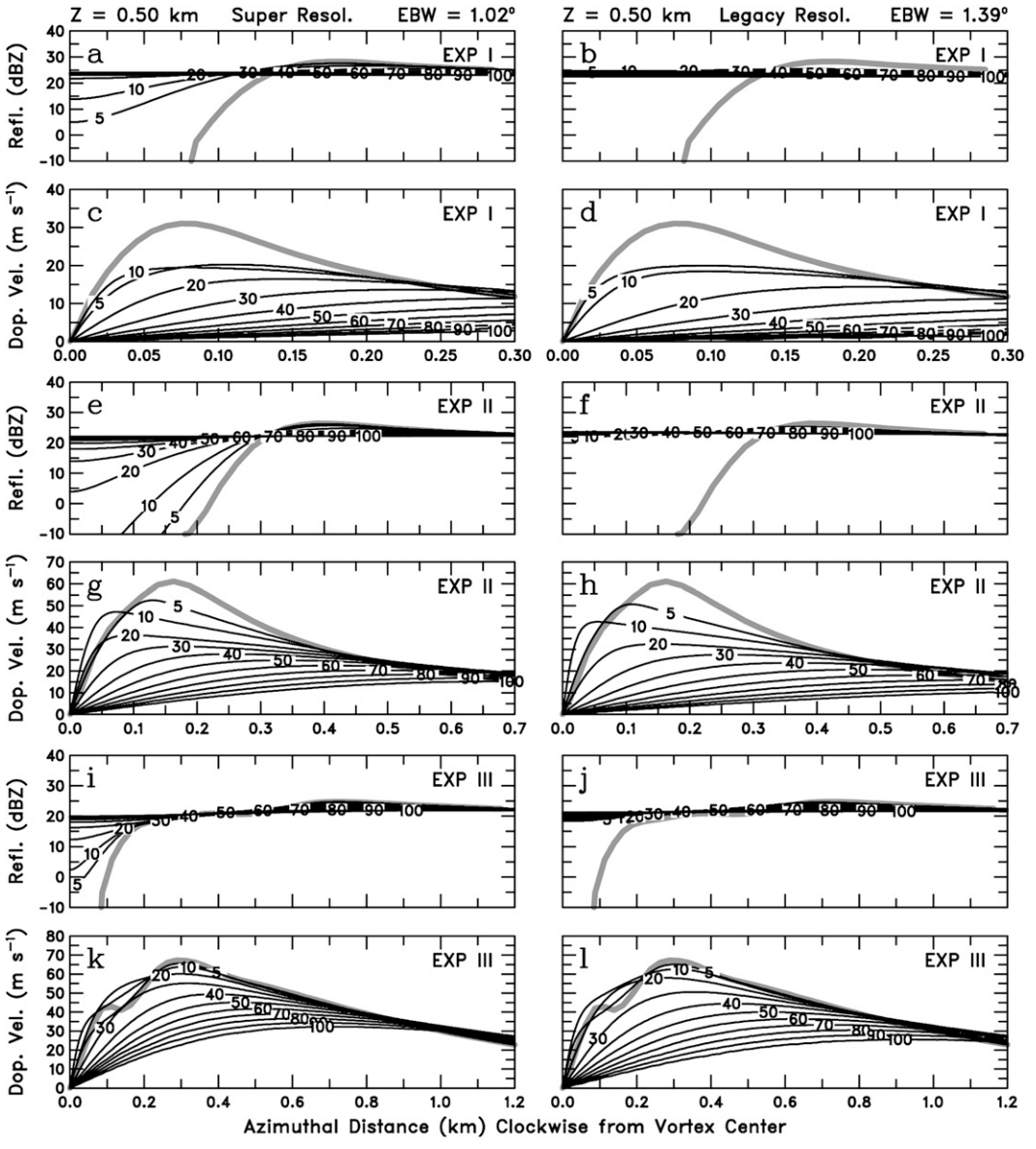

FIG. 12. Similar to Fig. 8, but with (a)–(d) showing the medium tornado (EXP I), (e)–(h) the large tornado (EXP II), and (i)–(l) the very large tornado (EXP III) at a height of 0.5 km. Note that the abscissa scales are different for each tornado.

marked differences resulting from the two sampling resolutions is evident in Fig. 2. The reflectivity sampling volume for legacy resolution is $1^\circ \times 1.0$ km, whereas the sampling volume for super-resolution is $0.5^\circ \times 0.25$ km, an increase of a factor of 8 in the sampling resolution.

As a reference, the bottom panels of Fig. 8 show how the Doppler velocity measurements respond to constant reflectivity values (20 dBZ) across the EXP II vortex. With increasing range from the radar, the Doppler velocity profiles are degraded in a consistent manner, with the peak value decreasing in magnitude and occurring at a greater distance from the vortex center. As expected, the degradation is more pronounced with legacy resolution than with super-resolution.

With nonuniform reflectivity across the tornado, however, the Doppler velocity profiles behave differently as a function of range (middle panels of Fig. 8). Within 20–30 km of the radar, the peak Doppler velocity values occur at a smaller radius than the actual core radius. It is not initially evident why this should be the case, but as will be discussed, it is due to the presence of the weak-reflectivity eye.

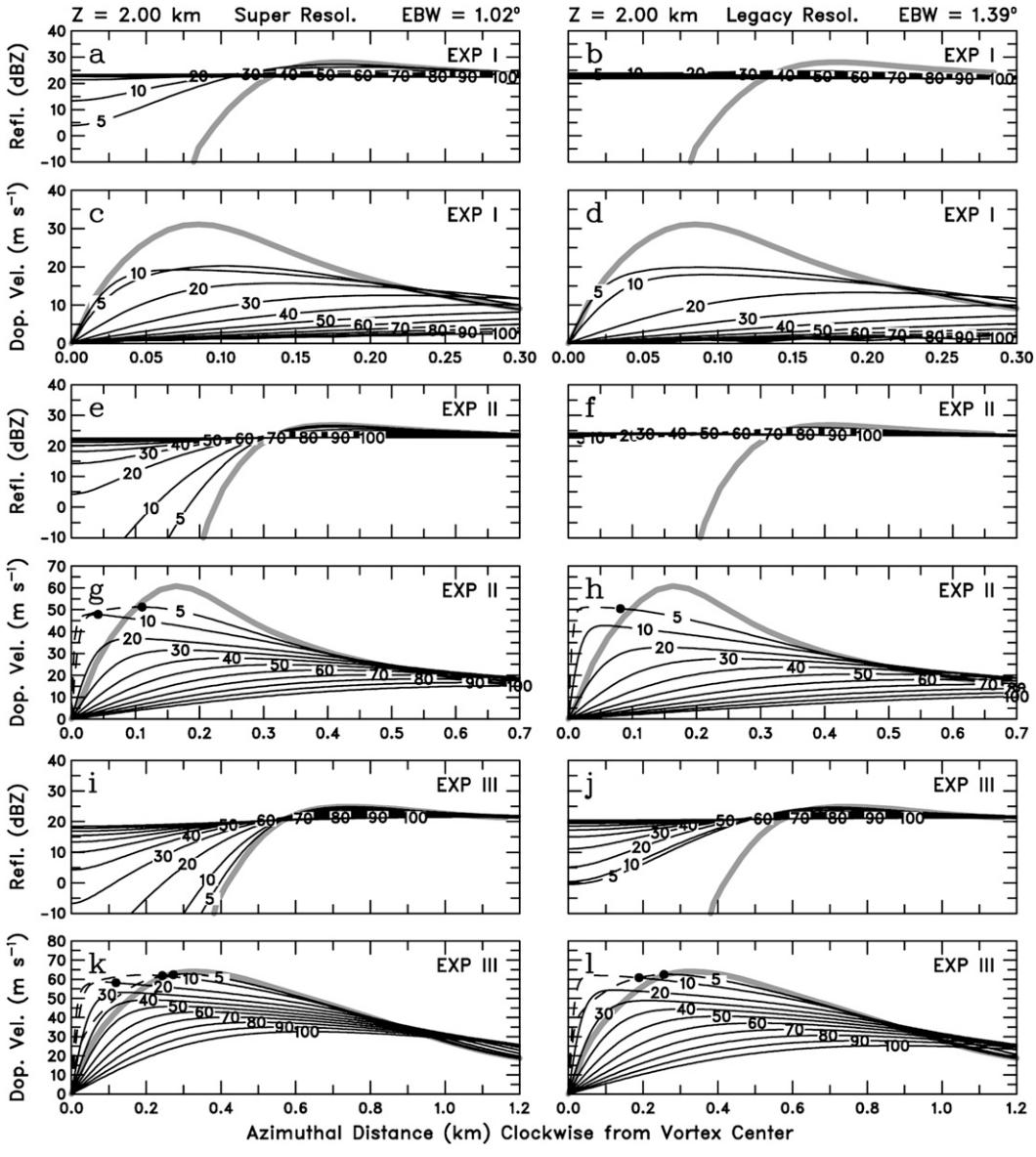

FIG. 13. Same as in Fig. 12, but for a height of 2.0 km. (e)–(h) As in Figs. 8a–d.

The plots in Figs. 9–11 were prepared in order to help understand the anomalous behavior of the Doppler velocity profiles in Figs. 8c and 8d at a range of 10 km from the radar. The center of a horizontal cross section through the radar beam is indicated by the black dot in the center of each panel. As one progresses through the top and bottom halves of Figs. 9–11, the radar scans across the EXP II tornado; it starts with the beam centered on the tornado and ends with the beam centered 0.4 km from the tornado center. The four panels in each half of Figs. 9–11 show, respectively, the distribution of reflectivity within the range and azimuthal extent of the beam in panels a and e, the distribution of the Doppler velocity values in panels b and f, the distribution of reflectivity weighted by the two-way antenna beam pattern in panels c and g (see appendix), and the distribution of the reflectivity-weighted Doppler velocity weighted by the antenna beam pattern in panels d and h. The mean Doppler velocity value within the beam is computed by dividing the sum of the values in panel d (panel h) by the sum of the values in panel c (panel g), represented mathematically in Eq. (A1).

When the beam is centered on the weak-reflectivity eye of the vortex (Figs. 9a–d), significant concentrations of hydrometeors are found only at the far edges of each of the sides of the beam (Fig. 9a). Consequently, the primary Doppler velocity values that are sensed by the radar (Fig. 9d) occur beyond the core region (dotted

circle in Fig. 9b) of the tornado. Because the positive and negative Doppler velocity values on both sides of the beam balance each other (Fig. 9d), the mean Doppler velocity within the beam is zero.

When the beam is centered 0.05 km to the right of vortex center (Figs. 9e–h), the concentration of scatterers is so small in the left portion of the beam (Fig. 9e) that the dominant reflectivity-weighted Doppler velocity values occur only in the right-most portion of the beam (Figs. 9g and 9h). The mean Doppler velocity value is assigned to the center of the beam, even though the mean value represents what is occurring along only one fringe of the beam. This, then, is the reason why the peaks of the mean Doppler velocity curves within a few tens of kilometers of the radar in Figs. 8c and 8d occur much closer to the center of the vortex than they would have if there were a uniform distribution of reflectivity across an EXP II–sized vortex (as in Figs. 8e and 8f).

The panels in Figs. 9–11 show that, as the beam center moves progressively away from the weak-reflectivity eye of the EXP II vortex, the locations of the Doppler velocity values that are represented by the mean Doppler velocity move progressively toward the center of the beam. When the beam center is 0.4 km from the center of the vortex, the main portion of the beam is outside the eye, so the reflectivity values weighted by the radial and azimuthal shapes of the beam are much closer to what they would have been had there been a uniform distribution of reflectivity.

5. Comparisons of Doppler radar signatures as a function of WSR-88D sampling resolution

Now that we understand how the presence of a weak-reflectivity eye and radar sampling affect mean Doppler velocity measurements across a tornado, we compare simulated Doppler radar measurements of the three numerically modeled tornadoes. Displayed in Figs. 12 and 13 are azimuth profiles of mean reflectivity and mean Doppler velocity across the tornadoes (clockwise from tornado center) as functions of range and radar resolution at heights of 0.5 and 2 km, respectively.

There are similar trends in reflectivity and Doppler velocity at both heights. The weak-reflectivity eye becomes less apparent with increasing range from the radar, but at a given range with super-resolution, the larger the tornado's eye, the more prominent the eye in the Doppler radar measurements. With the coarser sampling of the legacy resolution, the weak-reflectivity eye is apparent in the reflectivity measurements only for the very large tornado (EXP III) at heights above about 1 km.

In keeping with the arguments in the previous section, one notes that the range to which the radius of the peak

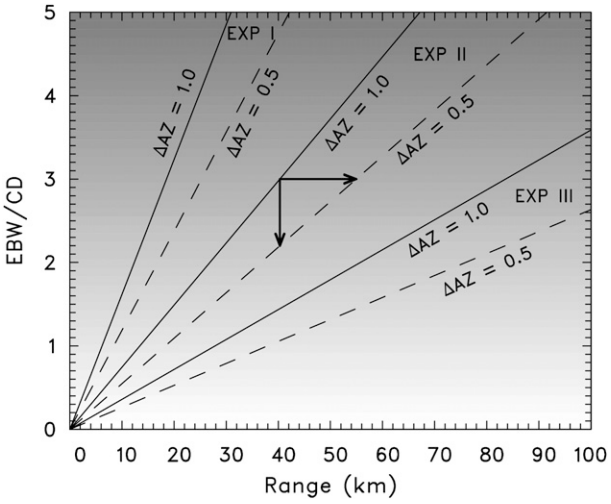

FIG. 14. Ratio of EBW to CD as a function of range from the simulated radar at a height of 1 km for the three tornadoes. Sloping solid and dashed lines represent the EBW/CD ratios corresponding to azimuthal sampling intervals of 1.0° and 0.5°, respectively. Grayscale gradation represents the smearing effects that increase with increasing EBW/CD ratio. At EBW/CD = 0, there is no smearing (i.e., perfect radar resolution). Boldfaced arrows are discussed in the text.

of the mean Doppler velocity curve underestimates the radius of the true peak increases with the increasing size of the weak-reflectivity eye. This effect is less pronounced with the legacy resolution than with the finer sampling of the super-resolution. In all situations, the peak value of the mean Doppler velocity curve decreases as the beam broadens with increasing range from the radar.

A close examination of Figs. 12 and 13 reveals that the width of the effective beam relative to the size of the tornado's core region controls the extent of degradation of the Doppler velocity profile; the wider the beam relative to the core diameter, the greater the amount of degradation. The curves in Fig. 14 represent the ratio of the effective beamwidth (EBW) to the core diameter (CD) as a function of range for all three experiments. For a given amount of degradation (as indicated by a given EBW/CD ratio), the distance from the radar to which a given amount of degradation is found increases with increasing tornado size (EXP I → II → III) and with increasing resolution (decreasing azimuthal sampling interval, ΔAZ).

The relationship between the 0.5° and 1.0° ΔAZ curves is summarized in Table 3. The range ratio of 1.36 for 0.5° super-resolution azimuthal sampling indicates that every 0.5° curve for a given resolution (EBW/CD ratio) is 1.36 times farther in range than the corresponding 1.0° ΔAZ curve. For EBW/CD = 3.0, the horizontal boldfaced arrow in Fig. 14 extends in range

TABLE 3. Relative effects of the azimuthal sampling interval (ΔAZ) on radar performance based on the mean characteristics of WSR-88Ds. [After Brown et al. (2002b).]

Resolution mode	One-way beamwidth (BW, °)	Effective one-way beamwidth (EBW, °)	Azimuth sampling interval (ΔAZ, °)	Range sampling interval (ΔR, m)	Ratio of resolution scale $\left(\frac{\text{EBW}}{1.39^\circ}\right)$	Range ratio $\left(\frac{1.39^\circ}{\text{EBW}}\right)$	Ratio of std dev estimate* $\left(\frac{1^\circ}{(\Delta\text{AZ})^{1/2}}\right)$
Legacy	0.89	1.39	1.0	1000 (Z) 250 (V)	1.00	1.00	1.00
Super	0.89	1.02	0.5	250 (Z,V)	0.73	1.36	1.41

* Assuming everything equal except the azimuthal sampling interval.

from 40 to 54.4 km (1.36 km × 40 km). Relative to the 1.0° legacy-resolution azimuthal sampling, the resolution scale is 0.73 for 0.5° ΔAZ sampling. For example, at 40-km range, the vertical boldfaced arrow indicates that the resolution (EBW/CD) decreases from 3.0 for 1.0° azimuthal sampling to 2.19 (0.73 × 3.0) for 0.5° azimuthal sampling. Though 0.5° azimuthal sampling results in increased resolution and increased range coverage at a constant antenna rotation rate, the standard deviation of the mean Doppler velocity estimate increases by an acceptable value of 1.41 (Table 3).

6. Conclusions

Legacy- and super-resolution Doppler velocity and donut-shaped reflectivity signatures associated with three tornadoes were produced using the high-resolution tornado numerical model of Dowell et al. (2005) and a simulated WSR-88D. Compared to legacy-resolution WSR-88D data, super-resolution data have an azimuthal sampling interval of 0.5° instead of 1.0° and a reflectivity range interval of 0.25 km instead of 1.0 km, while for both resolutions, the Doppler velocity range resolution is 0.25 km. As a consequence, super-resolution displays have twice the number of Doppler velocity data points and 8 times the number of reflectivity data points.

With the presence of the reflectivity eye at the center of a nearby tornado, Doppler velocity measurements had a peak velocity that was significantly closer to the tornado center than was seen in the model tangential velocity field. This distortion of the Doppler velocity profile was due to radar beams being positioned within the core region having negligible reflectivity-weighted Doppler velocity values within the eye. As a consequence, the only Doppler velocity values being averaged were those strong ones in the part of the beam at the edge of the core region. Therefore, one can expect the Doppler velocity values to peak at a smaller radius than the true radius of the tangential velocity maximum when the effective beamwidth is less than the tornado's true core diameter and there is a weak-reflectivity eye at the center of the tornado. As the beam becomes significantly wider with increasing range from the radar, the radius of the peak Doppler velocity values increases and the magnitude of the Doppler velocity values progressively decrease. At the same time, the eye reflectivity signature at the tornado center fills and eventually disappears.

Acknowledgments. The authors appreciate the efforts of Don Burgess and Lou Wicker of NSSL for reviewing and providing helpful comments and suggestions on an earlier version of this manuscript. Randy Steadham of Radar Operations Center and Dale Sirmans, Richard Ice, and David Warde of RS Information Systems provided information about the characteristics of WSR-88Ds. The authors also are indebted to Josh Wurman of the Center for Severe Weather Research and an anonymous reviewer for their valuable comments and suggestions that led to an improved manuscript. Development of the numerical vortex model used in this study was supported by the National Science Foundation under Grant 0437898. Funding also was provided by NOAA/Office of Oceanic and Atmospheric Research under NOAA–University of Oklahoma Cooperative Agreement NA17RJ1227, U.S. Department of Commerce.

APPENDIX

Calculations of the Doppler Velocity and Radar Reflectivity within an Effective Beamwidth

Here, we briefly describe a simulation procedure for calculating the mean (volume averaged) Doppler velocity ($\bar{V}_d$) and radar reflectivity ($\bar{Z}$) within the radar beam. Following the approach of Wood and Brown (1997), $\bar{V}_d$ is calculated as

$$\bar{V}_d = \frac{\sum_i \sum_j \sum_k V_{ijk} Z_{ijk} I_{ijk}}{\sum_i \sum_j \sum_k Z_{ijk} I_{ijk}}, \tag{A1}$$

where Z_{ijk} is the model reflectivity computed from the raindrop concentration in Eq. (1). In addition, V_{ijk} is the

undegraded Doppler radial component of a three-dimensional wind vector as a function of azimuth (i), range (j), and elevation (k) from a Doppler radar; V_{ijk} is given by

$$V_{ijk} = u_p \sin\gamma_i \cos\theta_k + v_p \cos\gamma_i \cos\theta_k + (w_p + V_T)\sin\theta_k, \quad \text{(A2)}$$

where u_p, v_p, and w_p are, respectively, the radial, tangential, and vertical components of the motion of hydrometeor particles (p) in relation to an axisymmetric vortex center. In (A2), γ_i ($\equiv \beta + \varphi_i$) is the angle between the radar-viewing direction (φ_i) and the tangential velocity component of the hydrometeor motion. The angle between east and the radial direction from the vortex center is β (positive in a counterclockwise direction). The terminal fall speed of hydrometeors is V_T (a negative quantity toward the ground) and is set equal to -5.4 m s^{-1}, corresponding to the 1.5-mm-diameter raindrops presented in this study.

In (A1), the composite weighting function of the antenna beam pattern (illumination I) is

$$I_{ijk} = \left|W(R_j - R_o)\right|^2 f^4(\varphi_i - \varphi_o, \theta_k - \theta_o), \quad \text{(A3)}$$

where φ_i, R_j, and θ_k are in the azimuth (i), range (j), and elevation (k) indices, respectively, within the beamwidth volume and φ_o, R_o, and θ_o are at the center of the beam. The elevation angle (θ_k) is the sum of the beam's elevation angle to the data point and the angle subtended by the verticals at the radar and at the measurement (i.e., data) point (e.g., Doviak and Zrnić 1993, p. 307). Note that the last term on the right-hand side of (A2) may be negligible at the lowest elevation angle presented in this study.

The weighting function $W(R_j - R_o)$ has the shape of a trapezoid in the range direction (Wood et al. 2001). The top of the trapezoid, where the weight is 1.0, has a range depth of 180 m. The base of the trapezoid, where the weight is 0.0, has a range depth of 260 m. The trapezoid-shaped pulse depth is the best fit to the WSR-88D pulse (D. Sirmans 2006, personal communication).

The two-way beam pattern f^4 ($\varphi_i - \varphi_o$, $\theta_k - \theta_o$) in (A3) is the antenna pattern (Gaussian) weighting function used to weight the model reflectivity factor values in the azimuthal and elevation directions within the resolution area and is given by

$$f^4(\varphi_i - \varphi_o, \theta_k - \theta_o) = \exp\left[-\frac{(\varphi_i - \varphi_o)^2}{2\sigma_\varphi^2} - \frac{(\theta_k - \theta_o)^2}{2\sigma_\theta^2}\right], \quad \text{(A4)}$$

where the standard deviations of the Gaussian density, $\sigma_\varphi^2[=\varphi_e^2/(16\ln 2)]$ and $\sigma_\theta^2[=\theta_3^2/(16\ln 2)$, are related to the half-power (-3 dB) beamwidth, and φ_e the horizontal effective half-power beamwidth, and θ_3 the vertical half-power beamwidth. Equation (A4) is a simple Gaussian function that has an approximate width of three one-way half-power beamwidths and neglects the effects of antenna sidelobes (Fig. 1). For summation computations in (A1) and (A5), the limits of the summation are $\varphi_i = \varphi_o \pm 1.5\varphi_e$ in the azimuthal direction and $\theta_k = \theta_o \pm 1.5\theta_3$ in the vertical direction. Additionally, the limits of the summation in the range direction are $R_j = R_o \pm 130$ m. For these simulations, the maximum number of data points within the beamwidth volume is $I = 101$ in the azimuth direction and $K = 101$ in the elevation direction, whereas the maximum number of data points in the range direction is $J = 25$.

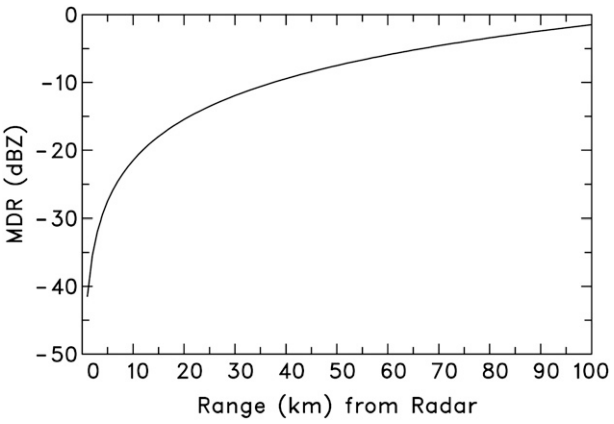

FIG. A1. Variation of the MDR with range for the short-pulse (precipitation) mode in the WSR-88D system. [After WSR-88D ROC (2007, 3–57).]

Radar reflectivity ($\bar{Z}$) within the radar beam may be expressed as

$$\bar{Z} = \frac{\sum_i \sum_j \sum_k Z_{ijk} I_{ijk}}{\sum_i \sum_j \sum_k I_{ijk}}. \quad \text{(A5)}$$

For the plots found in this paper, the mean radar reflectivity factor was converted to logarithmic radar reflectivity in units of dBZ as follows:

$$\text{dB}Z = 10\ \log\left(\frac{\bar{Z}}{1\ \text{mm}^6\ \text{m}^{-3}}\right), \quad \text{(A6)}$$

where the denominator refers to a reference value.

The minimum detectable reflectivity (MDR) for a given radar is a function of the lowest signal that can be detected; by definition, the lowest signal has a signal-to-noise ratio (SNR) of 1.0 or 0 dB. While SNR is independent of range, reflectivity is not. In simplified form, the weather radar equation can be written as

$$Z = Cr^2, \tag{A7}$$

where C is a constant specific to a given radar and r is the range from the radar (e.g., Battan 1973). For the WSR-88D, the MDR is specified as −7.5 dBZ at 50 km for the precipitation mode (WSR-88D ROC 2007, 3–57). Converting −7.5 dBZ to Z and substituting into (A7) at 50-km range, one determines that C is 7.11×10^{-5} $\text{mm}^6\ \text{m}^{-3}\ \text{km}^{-2}$. With C known, the MDR value can be computed from (A7) as a function of range (Fig. A1).

REFERENCES

Alexander, C. R., and J. Wurman, 2005: The 30 May 1998 Spencer, South Dakota, storm. Part I: The structural evolution and environment of the tornadoes. *Mon. Wea. Rev.,* **133,** 72–96.

——, and ——, 2008: Updated mobile radar climatology of supercell tornado structures and dynamics. Preprints, *24th Conf. on Severe Local Storms*, Savannah, GA, Amer. Meteor. Soc., 19.4. [Available online at http://ams.confex.com/ams/pdfpapers/141821.pdf.]

Battan, L. J., 1973: *Radar Observation of the Atmosphere*. University of Chicago Press, 324 pp.

Bluestein, H. B., 2005: A review of ground-based, mobile, W-band Doppler-radar observations of tornadoes and dust devils. *Dyn. Atmos. Oceans,* **40,** 163–188.

——, and A. L. Pazmany, 2000: Observations of tornadoes and other convective phenomena with a mobile 3-mm wavelength, Doppler radar: The spring 1999 field experiment. *Bull. Amer. Meteor. Soc.,* **81,** 2939–2951.

——, W.-C. Lee, M. Bell, C. C. Weiss, and A. L. Pazmany, 2003: Mobile Doppler radar observations of a tornado in a supercell near Bassett, Nebraska, on 5 June 1999. Part II: Tornado-vortex structure. *Mon. Wea. Rev.,* **131,** 2968–2984.

——, C. C. Weiss, M. M. French, E. M. Holthaus, R. L. Tanamachi, S. Frasier, and A. L. Pazmany, 2007: The structure of tornadoes near Attica, Kansas, on 12 May 2004: High-resolution, mobile, Doppler radar observations. *Mon. Wea. Rev.,* **135,** 475–506.

Brown, R. A., L. R. Lemon, and D. W. Burgess, 1978: Tornado detection by pulsed Doppler radar. *Mon. Wea. Rev.,* **106,** 29–38.

——, V. T. Wood, and T. W. Barker, 2002a: Improved detection using negative elevation angles for mountaintop WSR-88Ds: Simulation of KMSX near Missoula, Montana. *Wea. Forecasting,* **17,** 223–237.

——, ——, and D. Sirmans, 2002b: Improved tornado detection using simulated and actual WSR-88D data with enhanced resolution. *J. Atmos. Oceanic Technol.,* **19,** 1759–1771.

——, B. A. Flickinger, E. Forren, D. M. Schultz, D. Sirmans, P. L. Spencer, V. T. Wood, and C. L. Ziegler, 2005: Improved detection of severe storms using experimental super-resolution WSR-88D measurements. *Wea. Forecasting,* **20,** 3–14.

Burgess, D. W., M. A. Magsig, J. Wurman, D. C. Dowell, and Y. Richardson, 2002: Radar observations of the 3 May 1999 Oklahoma City tornado. *Wea. Forecasting,* **17,** 456–471.

Doviak, R. J., and D. S. Zrnić, 1993: *Doppler Radar and Weather Observations*. 2nd ed. Academic Press, 562 pp.

Dowell, D. C., C. R. Alexander, J. M. Wurman, and L. J. Wicker, 2005: Centrifuging of hydrometeors and debris in tornadoes: Radar-reflectivity patterns and wind-measurements errors. *Mon. Wea. Rev.,* **133,** 1501–1524.

Fiedler, B. H., 1993: Numerical simulation of axisymmetric tornadogenesis in forced convection. *The Tornado: Its Structure, Dynamics, Prediction, and Hazards, Geophys. Monogr.,* Vol. 79, Amer. Geophys. Union, 41–48.

Fujita, T. T., 1981: Tornadoes and downbursts in the context of generalized planetary scales. *J. Atmos. Sci.,* **38,** 1511–1534.

——, and R. M. Wakimoto, 1982: Anticyclonic tornadoes in 1980 and 1981. Preprints, *12th Conf. on Severe Local Storms*, San Antonio, TX, Amer. Meteor. Soc., 401–404.

Gunn, R., and G. D. Kinzer, 1949: The terminal velocity of fall for water droplets in stagnant air. *J. Meteor.,* **6,** 243–248.

Johnson, B. C., and C. L. Ziegler, 1984: Doppler observations and retrieved thermal and microphysical variables from the Binger tornadic storm. Preprints, *22nd Conf. on Radar Meteorology*, Zurich, Switzerland, Amer. Meteor. Soc., 31–36.

Lemon, L. R., D. W. Burgess, and L. D. Hennington, 1982: A tornado extending to extreme heights as revealed by Doppler radar. Preprints, *12th Conf. on Severe Local Storms*, San Antonio, TX, Amer. Meteor. Soc., 430–432.

Wakimoto, R. M., and B. E. Martner, 1992: Observations of a Colorado tornado. Part II: Combined photogrammetric and Doppler radar analysis. *Mon. Rev. Wea.,* **120,** 522–543.

——, W.-C. Lee, H. B. Bluestein, C. H. Liu, and P. H. Hildebrand, 1996: ELDORA observations during VORTEX-95. *Bull. Amer. Meteor. Soc.,* **77,** 1465–1481.

——, H. V. Murphy, D. C. Dowell, and H. B. Bluestein, 2003: The Kellerville tornado during VORTEX: Damage survey and Doppler radar analyses. *Mon. Rev. Wea.,* **131,** 2197–2221.

Wood, V. T., and R. A. Brown, 1997: Effects of radar sampling on single-Doppler velocity signatures of mesocyclones and tornadoes. *Wea. Forecasting,* **12,** 928–938.

——, and ——, 2000: Oscillations in mesocyclone signatures with range owing to azimuthal radar sampling. *J. Atmos. Oceanic Technol.,* **17,** 90–95.

——, ——, and D. Sirmans, 2001: Technique for improving detection of WSR-88D mesocyclone signatures by increasing angular sampling. *Wea. Forecasting,* **16,** 177–184.

WSR-88D ROC, 2007: WSR-88D system specifications. WSR-88D Radar Operations Center, ix + 142 pp. [Available from WSR-88D Radar Operations Center, 1200 Westheimer Dr., Norman, OK 73069.]

Wurman, J., 2002: The multiple-vortex structure of a tornado. *Wea. Forecasting,* **17,** 473–505.

——, and S. Gill, 2000: Superscale radar observations of the Dimmitt, Texas (2 June 1995), tornado. *Mon. Wea. Rev.,* **128,** 2135–2164.

——, and C. Alexander, 2004: Scales of motion in tornadoes, what radars cannot see, what scale circulation is a tornado. Preprints, *22nd Conf. on Severe Local Storms,* Hyannis, MA, Amer. Meteor. Soc., P11.6. [Available online at http://ams.confex.com/ams/pdfpapers/82353.pdf.]

——, and T. Samaras, 2004: Comparison of in-situ pressure and DOW Doppler winds in a tornado and RHI vertical slices through 4 tornadoes during 1996-2004. Preprints, *22nd Conf. on Severe Local Storms,* Hyannis, MA, Amer. Meteor. Soc., 15.4. [Available online at http://ams.confex.com/ams/pdfpapers/82352.pdf.]

——, J. M. Straka, and E. N. Rasmussen, 1996: Super-scale Doppler radar observations of tornadoes. *Science,* **272,** 1774–1777.